



Obtaining turbulence statistics of thermally driven anabatic flow by sonic-hot-film combo anemometer

Roni Hilel Goldshmid¹ · Dan Liberzon¹

Received: 26 December 2016 / Accepted: 12 November 2018 / Published online: 21 November 2018
© Springer Nature B.V. 2018

Abstract

Achieving a better understanding of atmospheric boundary layer flows, and of slope flows in particular, is of paramount importance for the research of climate processes and production of accurate weather forecasts. We addressed the need for high resolution statistics that describe the turbulence of thermally driven anabatic (upslope) flows by the implementation of a novel sonic-hot-film anemometer, the combo probe. A field experiment was staged to obtain continuous 8-day measurements of a thermally driven anabatic flow diurnal cycle on a moderate slope by a single combo probe mounted atop a 2 m high mast. Variations of the mean and fluctuating upslope velocity field components and temperature exhibit a strong correlation of the developing flow with the diurnal solar heating cycle. The provided detailed analysis of turbulence statistics includes characteristic length scales and spectra of velocity fluctuations almost up to the Kolmogorov scale. Identification of spectral shape similarity led to the introduction of a suitable normalization and comparison of the results to a theoretical model. Additionally, empirical fits of several parameters are produced and discussed with respect to variations of thermal forcing that were derived in terms of bulk temperature differences and buoyancy fluxes up the slope. The main outcomes are spectra resolved down to small scales and turbulence statistics made available for numerical simulations and future studies with slow instruments.

Keywords Anabatic flow · Combo probe · Thermal stratification · Turbulence spectra · Turbulence statistics

1 Introduction

Investigation of atmospheric boundary layer (BL) flows constitute a major part of climate research since they govern heat and scalar transport. Transport of contaminants therein directly influence microclimates by affecting cloud formation which set the precipitation regimes [1–4]. Atmospheric BL flows developing in complex terrains are the most convoluted and therefore difficult to investigate. Flows on hill and mountain slopes are mainly set in motion by thermal forces originating from diurnal heating/cooling cycles and appear

✉ Roni Hilel Goldshmid
rhilel@technion.ac.il

¹ Civil and Environmental Engineering, The Technion, 3200003 Haifa, Israel

in two configurations: anabatic (upslope) and katabatic (downslope) flows [5]. Many published studies cover various aspects of the more stable katabatic flows and significantly fewer published studies deal with turbulent anabatic flows, which evidences the relative difficulty to investigate upslope flows, especially experimentally. The major reason for difficulty of investigation is the lack of suitable instrumentation to cope with the inhomogeneity and non-stationary nature of the turbulent anabatic flow occurring from thermal forcing and resulting in buoyancy driven instabilities [5–7].

A variety of recent efforts were made in the field [8–13], in the lab [6, 14–17], and in numerical models [18–22] to examine thermally driven flows. The main approaches of examination included detecting, observing, and quantifying the important features of the flow such as: flow variability due to thermal forcing variations, buoyancy and momentum resulted mixing, dependence on slope geometry and roughness, and turbulence statistics. The observed features include eddy viscosity and thermal diffusivity causing rapid mixing and increased rates of heat/mass/momentum transfer as well as transport of pollutants [9]. Of high interest are the turbulent kinetic energy (TKE) dissipation rates and the finer scales of turbulent fluctuations, desirably down to the Kolmogorov length scale (η), uncapturable with the relatively slow instrumentation available in the field. Expanding our understanding of anabatic flow physics and gaining an insight of the turbulence structure of the flow is of paramount importance for weather and climate modelling and forecasting. However, obtaining comprehensive experimental data of the developing turbulent BL on slopes under various forcing and conditions is not trivial due to the transient nature of such flows. This obligatorily calls for development of new experimental instruments and techniques capable of obtaining continuous measurements at high spatial and temporal resolution in unstable conditions [23]. These must be compatible with complex natural conditions, including sometime hostile environments that complicate setting up meteorological towers, and must provide accurate data of the finest fluctuation scales in temporally transient anabatic flows.

Time series of velocity fluctuations are obtained from direct measurements, and their respective power density spectra provide all the necessary information for calculating turbulence statistics. Traditionally, the velocity flow field components are defined in a Cartesian coordinate system and are aligned with the probe or locally aligned with the slope. The instantaneous velocity field (u, v, w) can be decomposed into mean $(\bar{u}, \bar{v}, \bar{w})$ and fluctuating (u', v', w') components [24]. The current state of acceptable field work mainly presents the use of slow or low spatial resolution instruments such as ultrasonic anemometers (sonic) or LiDARS (light detection and ranging) hence limiting the detectable scale range of turbulent velocity fluctuations [25–29]. To the best of our knowledge, no comprehensive field data on high resolution velocity fluctuations of anabatic wind is available in the literature up-to-date. The natural solution for the lack of such data is the use of hot-wire/film anemometry as it can produce fine scale measurements of the velocity fields. Yet in harsh field conditions, it often means being stranded by the constant need of sensor recalibration due to changing temperature, changing humidity, inevitable contamination, and eventually degradation of the wire/film sensors. Additionally, the need for constant realignment of the hot-wire/film probes with the varying main flow direction renders the field use of hot-wire/film anemometers as especially cumbersome in such conditions.

A recently developed instrument consisting of collocated sonic and hot-film (HF) anemometers is the combo probe. It was originally proposed by Oncley et al. [30], and offers a solution for most of the listed above limitations. Modern sonic anemometers have the capability of sampling at up to 100 Hz, are relatively easy to operate, and do not require constant recalibration. However, their frequency response is highly dependent on the mean flow velocity, \bar{u} , due to the spatial averaging at relatively long fly paths of the acoustic

signal (usually ~ 10 cm). Kaimal and Finnigan [31] have shown that, for example, velocity field sonic measurements with mean velocity of 3.5 ms^{-1} have a trusted frequency response limited to 3.7 Hz (see Eq. 6.6 in [31]); contrarily, HF sensors are capable of capturing finer scale turbulence using a constant temperature anemometer (CTA). As the combo anemometer allows for concurrent detection of the field, its sonic provides velocity values at the low frequency range which are later used as the calibration set coinciding with the simultaneously detected voltages by the HF sensors. The in situ calibration is performed using neural networks (NN) trained to translate the given inputs (HF voltages) into outputs (velocities). Further details on the in situ calibration method adopted here are provided in Sect. 3. The combo design, its expected accuracy, and selection of suitable HF sensors have been evaluated in several recent studies [32–34]. These include laboratory work performed in a wind tunnel and a field study conducted in a stable stratified BL flow. The recent MATERHORN field campaign [13] included the first field use of combo probes where measurements of stable BL flows were successfully obtained during several weeks of continuous measurements with minimal human intervention.

On contrary to the first two reported field uses of the combo [13, 35], the main goal of this work was to demonstrate the ability of the combo probe to perform in highly transient thermally driven anabatic flow characterized by high levels of turbulence intensity (TI), and hence to begin addressing the lack of high resolution turbulence measurements of anabatic flow in general. The type of flow chosen for this purpose was the temporally transient upslope flow developing by the diurnal heating of a slope, which often occurs in hilly and mountainous terrains. The established suitable technique for the combo probe data collection and processing, in addition to the high resolution data set and the accompanying turbulence statistics, are made available for use in future field studies and in numerical and theoretical models pertaining to thermally driven flows on complex terrains.

Appropriate location and methods were chosen based on the considerations relevant to the selected flow and are elaborated in Sects. 2 and 3. Section 4 details the obtained results beginning with analysis of daily fluctuation averaged values and identifying the measured flow as an anabatic BL flow. The second part of the section provides detailed turbulent statistical properties of the velocity field. These results are additionally used to verify the ability of the combo probe to produce trustful measurements in such unstable conditions. Finally, empirical fits to the resolved spectral shapes and of some of the important turbulent properties are derived.

2 Observation site

A moderate slope located on the southwestern side of Nofit, a communal village in the northern part of Israel (32.7551°N , 35.1415°E), was chosen as the location of measurements due to its favorable topography and easily accessible power and communications. Situated on the low hills, some 15 km inland, the site is naturally shielded from possible offshore breeze. The time of year chosen for the measurements was in the peak of the 2015 summer, between August 8th and August 16th, to minimize anabatic flow perturbations by vegetation and to minimize the chances to encounter significant synoptic forcing. Indeed, during the 8 days of measurements, almost no cloud coverage and no synoptic systems were recorded.

The measurements were taken on the rocky slope with minimal vegetation, which encompassed only a few almost completely dry bushes of up to 0.5 m height at the time of

measurements and facing the southwestern side of the hill constituting a 5.7° slope. Google Maps[®] coordinates were used to derive the mean slope angle and the distance from the location of measurement to the street above, which was approximately 30 m and was partially obstructed by a line of houses. Further up across the street are several houses covering the slope up to the apex, at approximately 18 m up the slope from the location of measurements. The elevation variation between the point where measurements took place to the bottom of the slope was 7 m and the distance along the slope measured 70 m. The combo probe was mounted 2 m above the ground.

3 Instrumentation and data processing methodology

The site was instrumented with various probes and data acquisition equipment to allow continuous measurements of the 3D wind velocity field and the local distribution/concentration of common pollutants. In this work, only wind field results are reported. A single combo probe (Fig. 1), similar to the one used in [13, 35], was deployed atop a 2 m high mast providing high frequency measurements of all three velocity component fluctuations. The combo was composed of an ultrasonic anemometer by RM Young, model 81000, (hereinafter sonic) and two orthogonal X-shaped HF probes manufactured by TSI (model 1241-20W) that were mounted on a rotating holding arm. According to the method described below, the low temporal and spatial resolution velocity records of the sonic were used to perform the in situ calibration of HF voltages and for constant realignment of the HF probes with the mean wind direction. The latter was achieved by rotating (yaw rotation



Fig. 1 Measuring instruments: on the left side of the image are the AQMesh (pyramid shaped device) and the laser particle counter (inside the plastic cage); on the right side of the image is the combo including ultrasonic anemometer and the two X-shaped HF probes

only) the holding arm by a coupled stepper motor with a digital encoder (US Digital HD52A) providing radial accuracy of one tenth of a degree.

The sonic was programmed to sample at its maximum available rate of 32 Hz, providing an analog output of three velocity components (u , v , and w) and temperature (T). The sonic provided temperature was not used in this work, due to the lack of an additional anemometer that would provide temperature gradients, instead bulk air temperature fluctuations recorded by the two identical accurate temperature sensors described below were used. The HF sensors used in this field experiment (1.02 mm long and 0.05 mm wide each) are originally designed for liquid application and were selected for their higher robustness relative to the traditional thinner wires. One X-shaped HF sensor was oriented horizontally and the other vertically, hence providing voltage fluctuations across the films due to u , v and u , w velocity components respectively. The redundant information of the u velocity component was used to improve the signal-to-noise ratio of the main wind component, as the HF sensors were constantly realigned with the mean flow by means of averaging. The two sensors were stacked vertically to which improving the overall spatial resolution to just under 6 mm. The sensors were positioned just 2 mm off the sonic measurement volume center to avoid disturbance of the acoustic paths. Such configuration was previously tested in a wind tunnel and was found to be very reliable for measuring fine scale turbulence in natural atmospheric setups [34]. The HF sensors were driven by four MiniCTA channels (Dantec Dynamics model 54T42) with an overheat ratio set to 1.5. Yaw rotation of the HF sensors, placed several millimeters from the center of the sonic control volume, was performed in a way that the sensors themselves remain in place while only changing the direction to follow that of the mean wind calculated from the u and v sonic components. A specially written LabView routine collected data and controlled the combo. It ran on the mini field PC that was equipped with a National Instruments USB-6211 data acquisition board. Continuous recording of all combo data (four sonic, four HF, and one encoder channels) was performed simultaneously at a 2 kHz sampling frequency in 60-s long intervals. Once every 60 s an average wind direction of the last 5 s was calculated. It determined the next rotation angle and the new positioning of the sensors for the upcoming 60 s of measurements. Following the rotation, the actual new position was recorded from the readings of the encoder. Recalculation of new yaw position and the actual rotation of HF probes took no more than 0.7 s. The rotation angle, and hence the measurable angle of attack of the mean wind, was limited to a 120° span (centered at 240° meteorological angle) due to the geometrical restriction imposed by the sonic support struts. Accuracy expected from this combo depends on the mean wind velocity and was found to be sufficient using either two pairs of X shaped films, as done here, or a single V shaped 3D four wire sensor [34].

In addition to the combo sensing turbulent velocity field fluctuations, two air quality monitoring arrangements were installed at the site of measurements (left side of Fig. 1). Each included an AQMesh air quality monitoring system and a Dyllos laser particle counter (model DC1700). The two arrangements were set up at 2 and 0.2 m above ground and ~80 cm to the left of the Combo to avoid interference of the flow. The unit at 2 m height was set beside the combo and the unit at 0.2 m was set directly below the first. The AQMesh temperature records, were averaged over 15-min intervals and provided the main thermal stability data of the flow in terms of bulk temperature difference with an accuracy of 0.1 °C.

To derive the time series of velocity fluctuations from the HF voltages, a continuous in situ calibration against the slowly varying sonic data was implemented—based on the neural network (NN) training method established by Kit et al. [32]. After setting up the instruments in the field, data acquisition was recorded in 1-min long intervals continuously

for 8 days and resulted in series of records of the three velocity components provided by the sonic (at 32 Hz) and four HF voltages (at 2 kHz), all recorded simultaneously at 2 kHz. Hence, obtaining series of 120,000 data point long records from 60 s for each constituent. All sonic velocity records (u_s , v_s and w_s) were then translated into the HF probe coordinate system components (u_p , v_p and w_p) by

$$u_p = u_s \sin \alpha + v_s \cos \alpha, \quad (1)$$

$$v_p = -u_s \cos \alpha + v_s \sin \alpha, \quad (2)$$

α denoting the corresponding minute long record HF alignment angle, and $w_p = w_s$ was kept unchanged from the original records as the HF sensors performed only yaw rotation. Next, all data were examined to determine which minute long records are eligible for further processing by the NN based calibration method. Selection of eligible minutes was performed based on parameters established in [13, 32, 34], which included unidirectionality of the flow and mean flow direction relative to the current alignment of the HF sensors. Averages of each velocity component (\bar{u}_p , \bar{v}_p , \bar{w}_p) were calculated to select the eligible minutes for further processing. These are minutes during which the flow velocity was judged to be sufficiently “unidirectional” ($\bar{u}_p > 6\bar{v}_p$), aligned with the HF sensors with minimal deviation of less than 10° from the HF current orientation, and of mean wind speed above 2 ms^{-1} . The average vertical velocity component \bar{w}_p was found always to be significantly smaller than \bar{u}_p . The selected records were split into groups not exceeding 1 h of total time span during which the temperature fluctuations did not exceed $\pm 2^\circ \text{C}$. Figure 3, later in the text, depicts the total amount and the spread of processed eligible minutes along all 8 days of measurements.

The HF sensed velocity field records were derived using in situ calibration of the HF voltages with NN based velocity voltage transfer functions [32], where each transfer function was reliable for an ensemble of eligible minutes constituting a single hour. Since the sonic and HF simultaneously sense the same flow field, a low pass filter can bridge the variation in spatial and temporal resolutions and enable both instruments to provide the same outputs at low frequencies. The low pass filtered data was hence used as a training set (TS) constituting inputs (HF obtained voltages) and targeted outputs (sonic obtained velocities) to train the NN. Each TS consisted of five selected minutes that best represented the entire range of recorded data within the single currently processed hour. Determination of best representation was established by selecting the minutes whose mean velocities, \bar{u} , formed an ensemble of five average velocities that spread across the entire \bar{u} range of that hour. Each TS data point consisted of four HF voltages and their respective three velocity components from the sonic, with 600,000 data points in total. Low pass filtering was then performed by block averaging the TS data into 600 data point blocks, which is equivalent to the trusted sonic output range at a lower cut off frequency of 3.3 Hz. Finally, each hour of data had its characteristic TS of 1000 data points that was used to produce the transfer function.

The transfer function for each hour was composed of two independent NN, one for each HF sensor to increase the signal-to-noise ratio of the main component, u , of the flow. The first NN was used to derive u_p and v_p from the horizontally oriented HF sensor u voltages and the second for u_p and w_p from the vertically oriented one. After the two NN were trained for every hour, velocities were derived for all sufficiently “unidirectional” minutes previously selected within that hour. Next, the time series of the main velocity component u_p from both NN were averaged and provided records with higher signal-to-noise ratio. Finally, the derived velocity time series were examined and turbulence statistics such as:

TI, TKE, velocity derivative skewness (Sk), TKE dissipation rates (ϵ), η , and the power density spectra of velocity fluctuations were produced.

4 Results

The results below are divided into two parts: the first presents the diurnal fluctuations using mean flow analysis and the second provides a detailed analysis of high resolution turbulence statistics.

4.1 Meteorology of anabatic flow

First, we examined records of diurnal variations. Figure 2 presents the summary statistics of the mean along slope velocity component, mean wind direction, mean temperature, and temperature difference ($\Delta T = T_{2m} - T_{0.2m}$) at two elevations. The velocity mean quantities

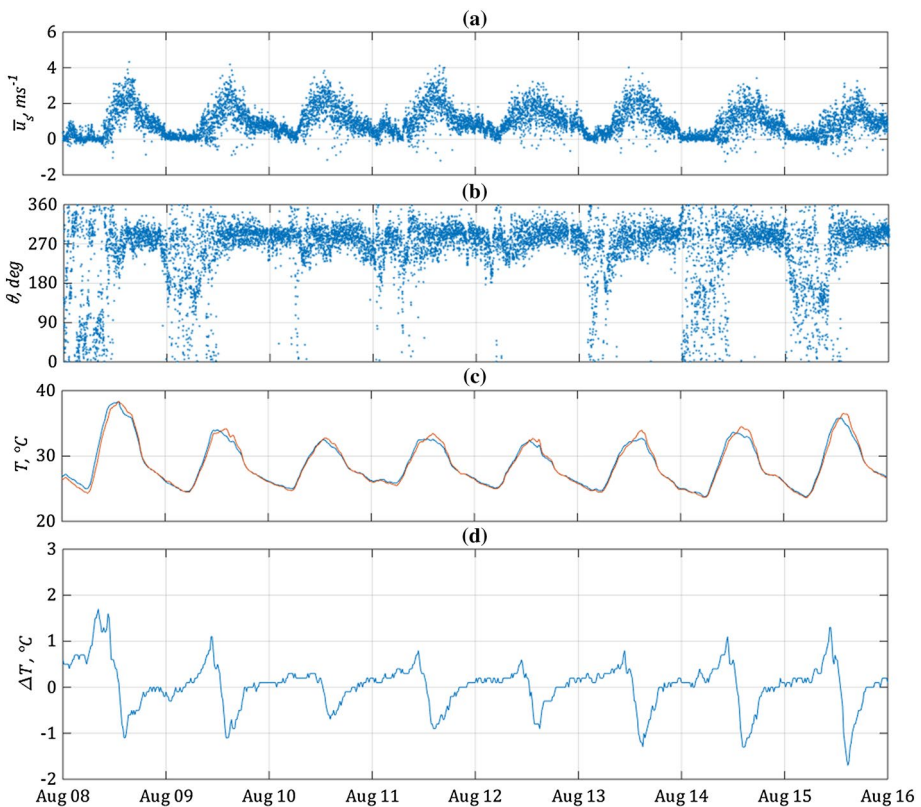


Fig. 2 Eight-day long data records: **a** mean along slope component of wind speed (\bar{u}_s) of every recorded minute; **b** meteorological direction (θ) of the wind; **c** AQMesh temperature (T) at 2 m above the ground (in blue) and just above the ground (in orange); and **d** AQMesh temperature difference fluctuations ($\Delta T = T_{2m} - T_{0.2m}$). Date ticks on the horizontal axis correspond to midnight (00:00 h)

are 1-min averages measured by the sonic, and the temperature quantities are 15-min averages measured by the AQMesh instruments.

The wind speed and direction followed a diurnal pattern strongly correlated with the temperature variations and the slope alignment. The mean wind direction during day hours flowed up the slope ($\theta \approx 280^\circ$) and its peaks occurred at the ΔT minima, i.e. corresponding to the periods of unstable stratification maxima. This indicates the development of a thermally driven anabatic flow. The broad range of mean velocity values observed in this study, along with the turbulence statistics analyzed below, suggests that the upslope flow in the BL is highly turbulent and a suitable normalization may assist in clarifying the diurnal pattern. Therefore, 1-min mean wind speed normalized by the respective daily maximum values for all 8-day measurements are plotted in Fig. 3. The daily maxima (\bar{u}_{smax}) used for normalization were derived from eight mean along slope velocity distribution curves independently fitted into each daily ensemble (as in Fig. 2a). The normalized ensemble distribution forms a distinctive pattern, and a normalized diurnal curve was fitted (shown as a solid red curve in Fig. 3) to represent it. Each day begins with an increase from virtually zero motion shortly before sunrise, followed by a rapid increase in wind speed until the maximum is attained at early afternoon. A gradual decrease of the mean wind speed toward sunset concludes the cycle. Direction of the mean flow is given in Fig. 2b. The observed diurnal pattern is in agreement with Demko et al. [10]; however, the maximum mean velocities observed here are much higher, reaching values of 3–4 ms^{-1} . Outside daylight hours, no significant downslope flow was recorded. One possible reason is partial

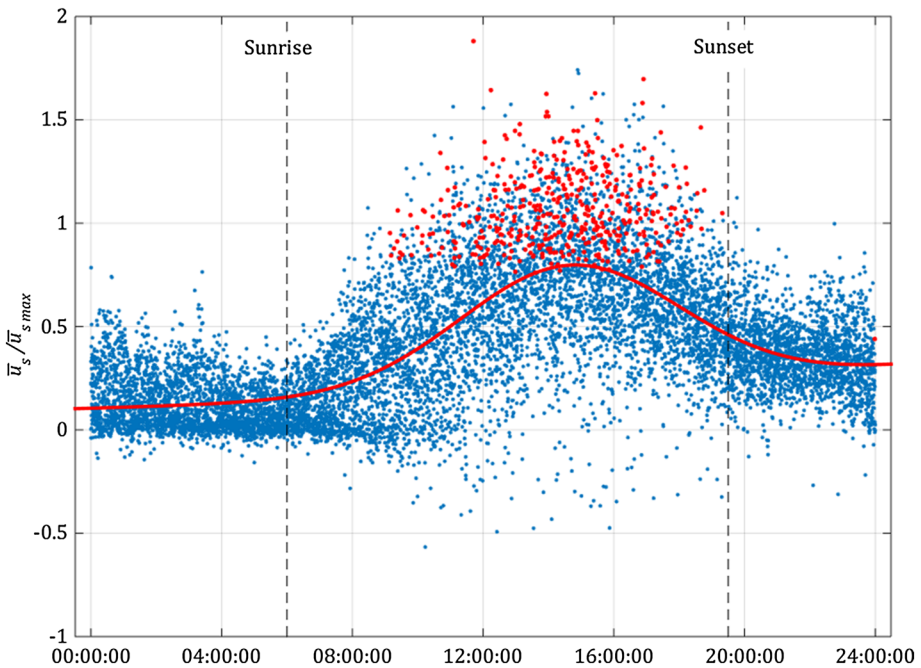


Fig. 3 The normalized average along slope velocity ($\bar{u}_s / \bar{u}_{smax}$) ensembles representing the diurnal cycle during the days of measurement at local time. The red curve represents a fit of the normalized average velocities of all 8 days, and the red dotted ensemble represents the minutes found eligible for NN based calibration and processing

obstruction by the houses positioned higher up the slope that may prevent katabatic flow development, however low altitude katabatic flow forming as low as 1 m above the ground is another possibility [36].

Observing a clear diurnal fluctuation pattern of both the upslope wind velocity magnitude and direction, accompanied by that of the bulk temperature gradient, the main driving force of the upslope flow was to be determined. The option of sea breeze was examined first. This was achieved by comparing the observed patterns at the measurement site with wind magnitude and direction fluctuation data available at surrounding metrological stations during the same 8 days of measurements. Four nearby stations were considered, some exposed to the sea and some blocked by the topography, similar to the slope at Nofit. Figure 4 presents the four station locations on a map, while Fig. 5 displays the diurnal changes of the mean wind magnitude and direction. Three stations are operated by the Israel Ministry of Environmental Protection, namely Kiryat Ata (32.8115°N, 35.1123°E), Kfar Hasidim (32.7426°N, 35.0944°E) and Daliyat al-Karmel (32.6811°N, 35.0698°E). Data from the station located at Neve Ya'ar (32.7078° N, 35.1784° E) were provided by the IMS (Israel Meteorological Service). The Kfar Hasidim station available data was limited to the last 2.5 days corresponding to this study period. Three of the stations, excluding Neve Ya'ar, showed clear periodic diurnal fluctuations, with the wind mean velocity aligning at a specific meteorological angle and reaching respective daily maximum during the light hours. In absence of significant synoptic forcing, the flow at each of the examined stations could be associated with the sea breeze, and hence the relevant wind path topography was examined and compared with that of the site of measurements at Nofit. The topographies from the sea to each of the stations along the path corresponding the mean wind direction were plotted in Fig. 4a–e. It was noted that at stations not blocked from the sea by topographic features the mean wind direction during the day hours corresponded with the expected sea breeze direction. It was at $\sim 286^\circ$ at the Kiryat Ata station located north of Mount Carmel in the Haifa Bay area, and at $\sim 320^\circ$ at Kfar Hasidim located further South, inland, and close to Nofit. On contrary, the mean wind direction recorded at shielded by topography Daliyat al-Carmel station on the Mount Carmel was $\sim 309^\circ$, higher than the expected sea breeze direction. The Neve Ya'ar station, positioned close to Nofit and in similar topography but situated at the hill apex, experienced winds at $\sim 293^\circ$, an angle smaller than the expected sea breeze direction recorded at the nearby Kfar Hasidim station. At the measurement site, the mean wind direction was at $\sim 280^\circ$, also smaller than the expected sea breeze wind direction. Both the Nofit slope and Neve Ya'ar stations are blocked from the sea in the direction of the recorded mean wind flow by topographic features, mainly the Mount Carmel reaching altitude exceeding 400 m above sea level. It was hence concluded that wind measured on the slope at Nofit was not sea breeze, but locally forced upslope flow.

After refuting sea breeze as a driving mechanism, the diurnal behavior of the flow was further examined in terms of on the slope bulk temperature gradients. The representative average velocity curve is plotted against the normalized temperature differences $\Delta T/\Delta T_{\min}$ and against the mean upslope buoyancy flux curve in Fig. 6. The temperature differences were normalized using the obtained daily minima since it best represents the maximum daily unstable stratification, or the driving mechanism of the upslope flow. Relying on single point measurements, the true Richardson number could not be calculated because velocity gradients are unattainable. Instead, the Reynolds number (Re) based on η was chosen to allow future comparisons with data obtained in similar setups. As the slope lengths and mean velocities may change significantly in natural setups, the Re value range is large. However, using a turbulence characteristic length scale will allow comparison with

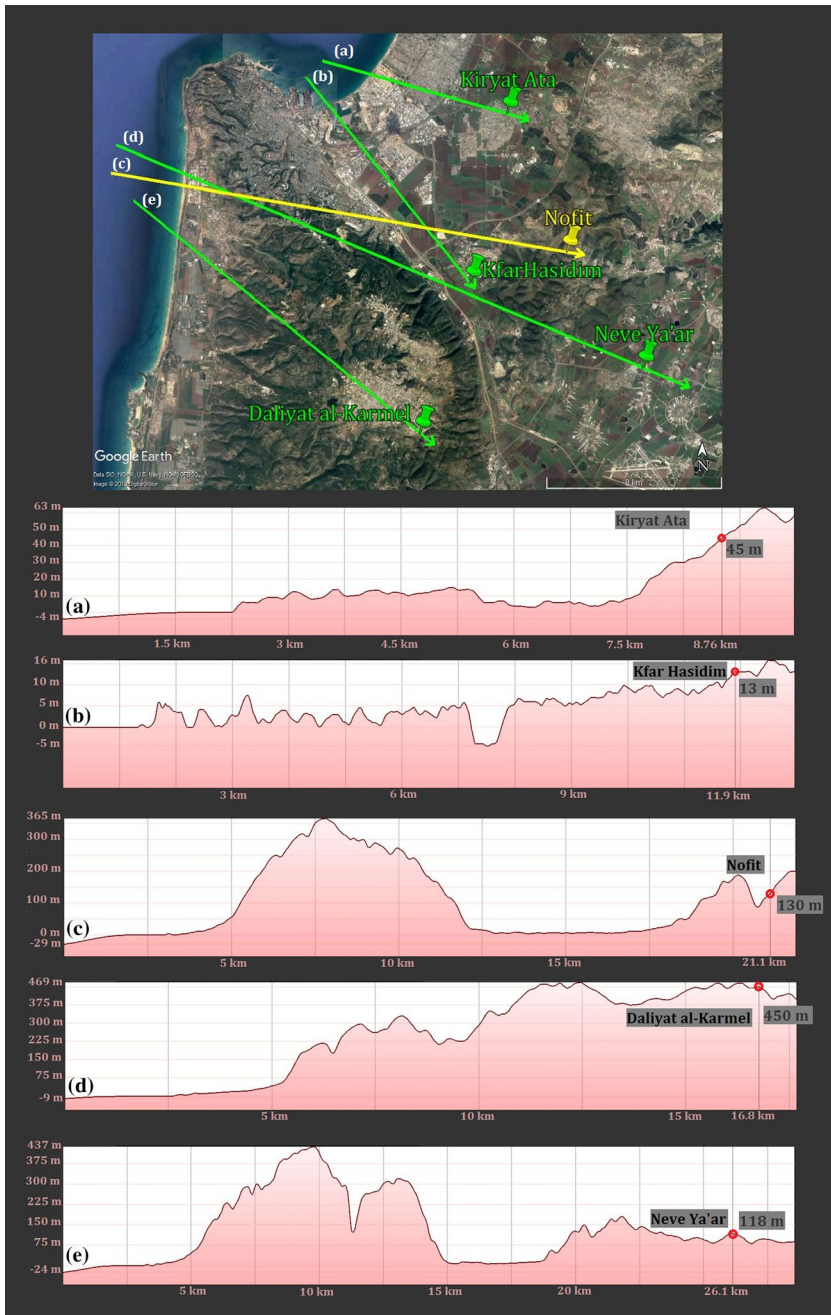


Fig. 4 A map of the meteorological station locations and topography graphs depicting elevation variations along the path from the sea to each station. The red circles indicate the actual station locations and their relative height above sea level. The path is in the direction of the mean wind as measured during the time period corresponding to that of the eligible minutes at the Nofit measurement site. The wind direction of each graph corresponds to the mean wind direction of: **a** Kiryat Ata $\sim 286^\circ$; **b** Kfar Hasidim $\sim 320^\circ$; **c** Nofit $\sim 280^\circ$; **d** Daliyat al-Karmel $\sim 309^\circ$; **e** Neve Ya'ar $\sim 293^\circ$

flows both in nature and the lab, and allow comparison with unstable stratification forced turbulent flows not necessarily over slopes. This is elaborated in more detail in Sect. 4.2. Additionally, the upslope buoyancy flux was calculated by

$$\bar{b} = g \frac{T_{0.2m} - T_{2m}}{T_{0.2m}} \bar{u}_{upslope} \quad (3)$$

where $\bar{u}_{upslope}$ is the mean velocity obtained by the sonic after rotating all velocity components 280° about the z-axis and 5.7° about the y-axis. The mean curve obtained by averaging the upslope buoyancy flux values from all 8 days is also plotted in Fig. 6. The upslope flow buoyancy flux, calculated using the upslope velocity as in [37], was selected to examine the flow dependence on buoyant forcing, as opposing to the turbulent buoyancy flux. This is due to the lack of high frequency temperature measurements that could be used in combination with the HF acquired high frequency vertical velocity component records, and the inability to use sonic provided temperature fluctuations for the reasons discussed earlier in the text.

The pattern observed in Fig. 6 further points toward the existence of thermally forced unstable stratification of the air on the slope, setting the anabatic flow in motion. Immediately after sunrise, the solar heating of the slope surface and the appearing buoyancy forces formed a turbulent BL of anabatic flow [38, 39]. In Fig. 6, all 8-day data ensembles indeed showed a similar behavior reaching respective daily maximum value shortly after noon, almost simultaneously with the mean wind speed maximum and maximum 8-day mean upslope buoyancy flux. Normalized temperature differences, upslope buoyancy forces, and mean velocity variations were strongly correlated, again indicating the presence of thermally induced anabatic flow.

One-minute long mean buoyancy fluxes were also plotted against the corresponding meteorological angle values to further demonstrate the convergence of the flow direction up the slope due to formation of buoyant instability. The upslope buoyancy values are positive when the mean flow direction is up the slope and unstable stratification is present. These values are negative when unstable stratification begins, i.e. $\Delta T > 0$ and the slope of $\Delta T > 0$ as well. Otherwise, the wind direction is scattered. Additionally, the direction of the flow converges to $\theta \approx 280^\circ$ when upslope buoyancy flux increases.

These combined figures (Figs. 2, 3, 4, 5, 6, 7) suggest the flow is indeed thermally driven. Figures 4 and 5 display the surrounding meteorological stations data along with topography details to rule out the possibility of the sea breeze or synoptic pressure gradients—due to the lack of diurnal variability in surrounding stations. As Fig. 6 displays the flow direction adjustment in correlation with the bulk temperature gradient and the upslope buoyancy flux increase, it thoroughly summarizes the diurnal cycle. During the night, the temperature gradient is virtually zero, i.e. neutral stratification. As the sun rises, the slope and adjacent air masses begin to heat up, initiating air motion. Although the initial stratification is stable, reaching maximum stability around 10:30, low mean upslope velocities are recorded (Figs. 2, 3) along with significant fluctuations of the mean flow direction—represented by a large scatter (Figs. 2, 7). This scatter is expected because the slow air motion with strongly fluctuating direction mixes the surrounding air masses. From 10:30 the stable stratification begins to break up, rather rapidly, changing into unstable stratification. During this process the scatter in the flow direction decreases and the mean upslope velocity magnitude begins to increase. Only after the temperature gradient becomes that of unstable stratification the upslope velocity reaches its close to maximum values and remains at this level for several hours. Alignment of the flow with the upslope direction, as seen in

Fig. 5 Mean wind magnitude and direction variations at each of the four meteorological station. The data corresponding to time periods with eligible minutes, as observed at the site of measurements in Nofit (9:00–20:00), are marked in red. The solid black line indicates the Nofit observed upslope flow direction of 280° . **a1** Kiryat Ata 30-min mean wind direction; **a2** corresponding mean wind speed. **b1** Kfar Hasidim 30-min mean wind direction; **b2** corresponding mean wind speed. **c1** Daliyat al-Carmel 5-min mean wind direction; **c2** corresponding mean wind speed. **d1** Neve Ya'ar ten-min mean wind direction; **d2** corresponding mean wind speed

Fig. 2b, occurs simultaneously with flow direction scatter reduction. The flow becomes significant and its direction aligns along $\sim 280^\circ$ (up the slope). In the evening hours, towards sunset, the slope heating gradually diminishes, the unstable stratification begins to break up accompanied by the gradual reduction of the upslope flow magnitude. The velocity magnitude is reduced to very low values after sunset when the stratification, in terms of temperature gradient, becomes neutral. Such variations in flow direction at low magnitudes evidence the ongoing change in the stratification pattern. The combination of these data shows the examined upslope flow was indeed driven by the unstable stratification developing over the slope due to solar heating during the day. The results are not canonical and exhibit scatter and fluctuations, as expected at a non-perfectly uniform and smooth slope that is not oriented perfectly to the south.

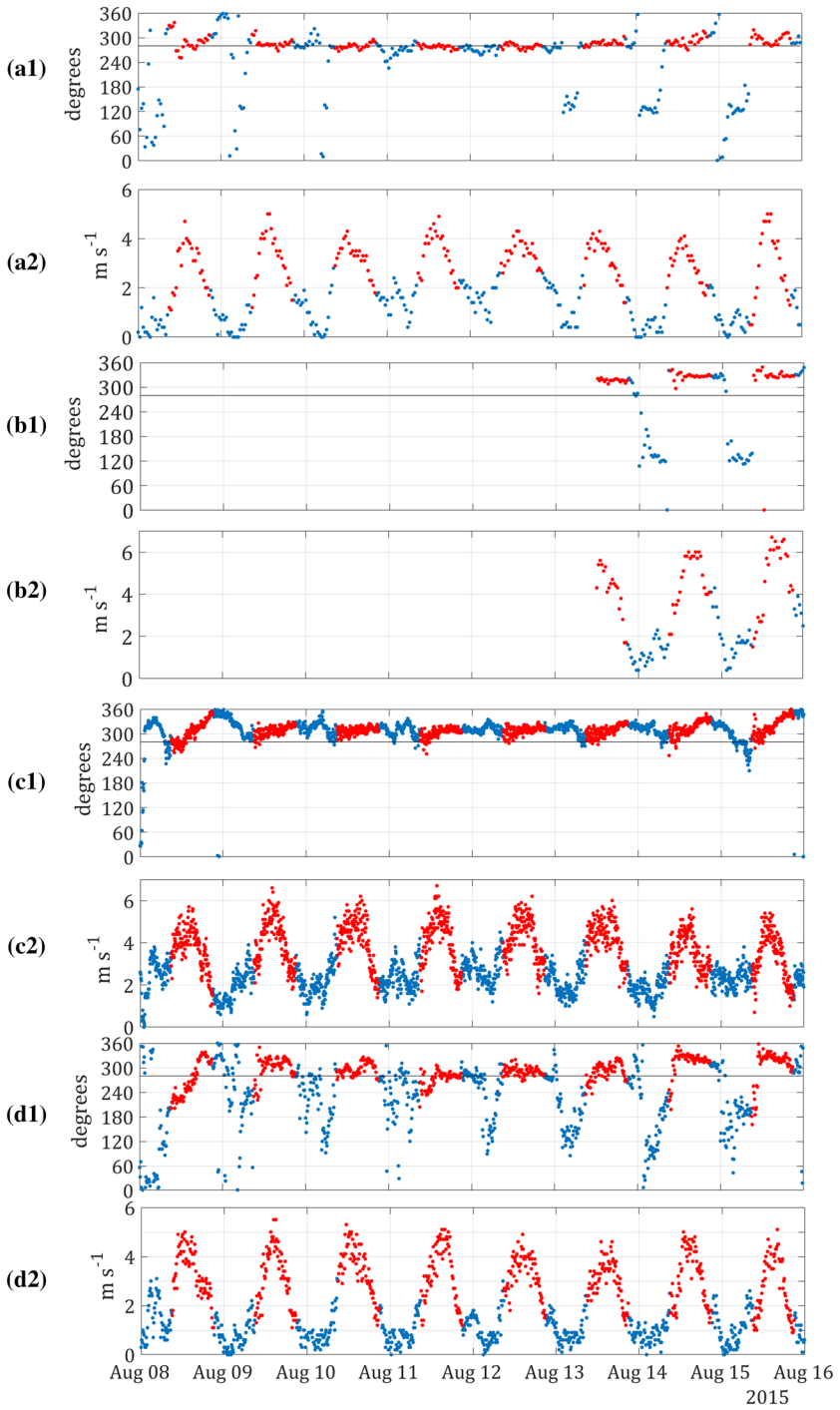
After establishing the diurnal pattern of the examined flow and its dependence on the daily thermal forcing, the alignment of the flow with the slope was examined. Mean flow alignment with the slope was detected at approximately 5.7° when mean velocities were higher than 2 ms^{-1} . The alignment corresponds well with the chosen threshold for eligible minute long records used for high frequency turbulence analysis, which is elaborated in the following section.

4.2 High resolution turbulence of anabatic flow

Further elaborated analysis of the turbulent flow statistics was performed adopting a slope aligned coordinate system. For that purpose, all HF velocity records, obtained by the described above in situ NN calibration, were translated by 5.7° to the horizontal following the initial translation to follow the direction of the probe, as mentioned in (1–2). As a result, u is aligned with the slope, v transverses the slope component, and w is the component normal to the slope surface when velocities climb over 2 ms^{-1} .

Examination of turbulence statistics as obtained by the combo records was performed by calculating the power density spectra of velocity fluctuations and various statistical parameters of the time series: namely TI , TKE , Sk , and average TKE dissipation rates ($\bar{\epsilon}$). The kinematic viscosity of air in the recorded temperatures was taken to be $\nu = 1.6 \times 10^{-5} \text{ m}^2\text{s}^{-1}$. The resulting turbulence statistical dependence on Reynolds number (Re), instead of the Richardson number, were presented where appropriate due to the absence of a lower anemometer. The thermal forcing effects were instead discussed based on the recorded bulk (vertical) temperature differences.

Using the in situ calibration of the HF sensor provided velocity fluctuations at a high sampling frequency of 2 kHz, and the power density, P - f , spectra of all three velocity components were calculated for all available 1-min data sets. Spectra were obtained by performing windowed Fourier Transform calculation in 2.048-s long windows. This effectively produced averaged power spectra of each 120,000 long 1-min record at 0.4882 Hz frequency resolution. Figure 8 below presents the spectra of four representative measured minutes from August 9th and August 10th. All obtained velocity



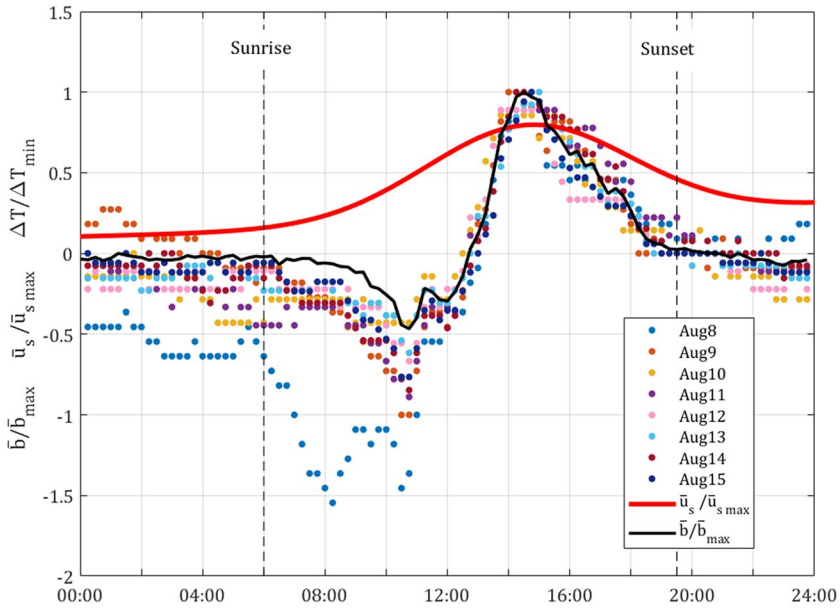


Fig. 6 Daily temperature difference (ΔT) fluctuations normalized to the respective daily minimum. Red curve is the normalized average velocities curve. Black curve is the normalized 8-day average upslope buoyancy flux. Sunrise of each of the 8 days occurred at 06:00 and sunset occurred at 19:30 local time

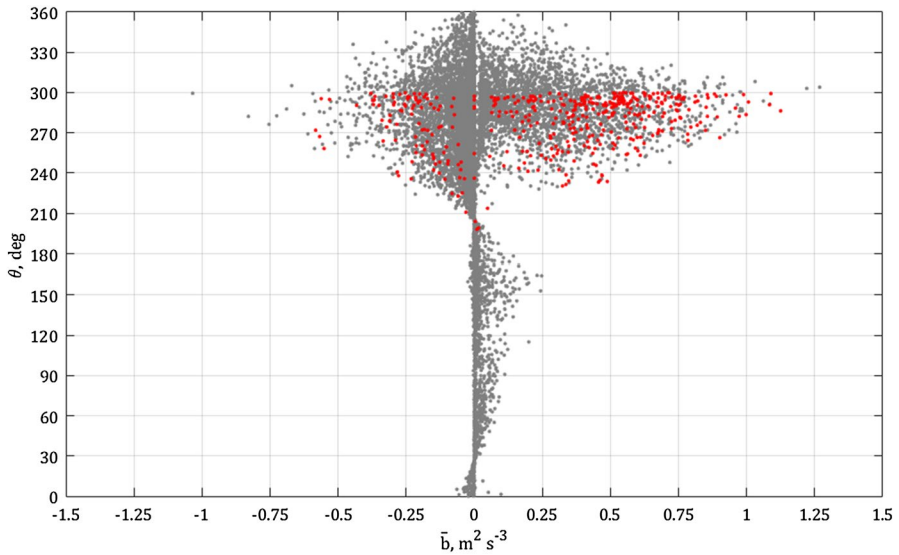


Fig. 7 Meteorological angle plotted against buoyancy flux of all recorded minutes in grey, and eligible (explained above as minutes suitable for processing) minutes in red

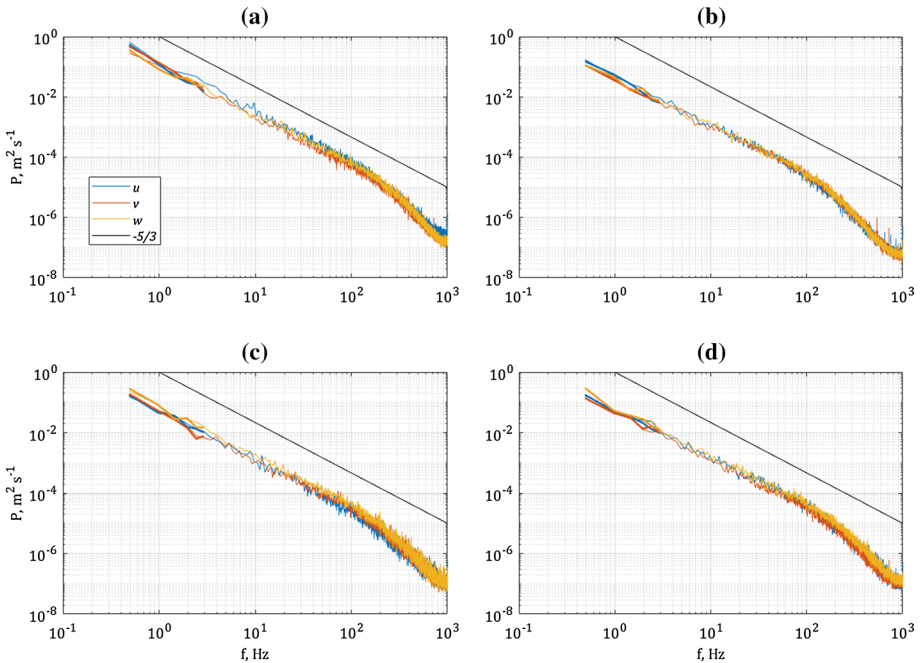


Fig. 8 The velocity fluctuation power density spectra of four independent minutes along with their respective turbulence statistics. The thicker lines indicate the sonic obtained data translated to the same coordinate system aligned with the slope. **a** August 9th at 3:08 p.m. $TI=32.7\%$, $TKE = 1.586 \text{ m}^2 \text{ s}^{-2}$, $Sk_u=-0.350$, $\bar{\epsilon}=0.105 \text{ m}^2 \text{ s}^{-3}$, $Re_\eta=107.1$. **b** August 9th 4:17 p.m. $TI=29.4\%$, $TKE=0.493 \text{ m}^2 \text{ s}^{-2}$, $Sk_u=-0.551$, $\bar{\epsilon}=0.082 \text{ m}^2 \text{ s}^{-3}$, $Re_\eta=70.5$. **c** August 10th at 11:17 a.m. $TI=30.8\%$, $TKE=0.814 \text{ m}^2 \text{ s}^{-2}$, $Sk_u=-0.267$, $\bar{\epsilon}=0.087 \text{ m}^2 \text{ s}^{-3}$, $Re_\eta=85.2$. **d** August 10th at 3:10 p.m. $TI=31.7\%$, $TKE=0.796 \text{ m}^2 \text{ s}^{-2}$, $Sk_u=-0.497$, $\bar{\epsilon}=0.109 \text{ m}^2 \text{ s}^{-3}$, $Re_\eta=77.4$

fluctuation spectra presented rather similar shapes as in Fig. 8: the inertial subrange has a constant slope and the dissipation subrange is clearly pronounced.

In approximately 15% of the examined minute long spectra, the transition to the dissipation subrange was characterized by a large “bulge” (Fig. 9b, d), indicating the presence of a so called “bottleneck” effect [35, 40–42] appearing at ~60 Hz. Figure 9a, c present visual examinations of the corresponding velocity fluctuation time series and revealed the presence of velocity bursting that is manifested as a local increase of fluctuation intensity. Similarly, in the MATERHORN [35] field campaign that was conducted in Dugway Proving Grounds, Utah USA, the combo was used as the measuring instrument. Unlike this work that examines unstable BL flows, they examined stable BL flows and noticed both the presence of the bottleneck bump on the spectra at ~100 Hz and the visual representation of bursting in the corresponding time series. The bursting phenomenon is common in thermally driven flows and can be the result of several mechanisms. Some believe that bursting is of great importance because it is one of the primary energy generation mechanisms in the BL [43, 44]. The ability to capture bursts in a natural BL of relatively low mean speed is highly advantageous and is conceivable due to the use of the combo. Influence of burst presence on the spectral statistics is elaborated below, while a detailed discussion of burst generation mechanisms was left outside of the scope of this work.

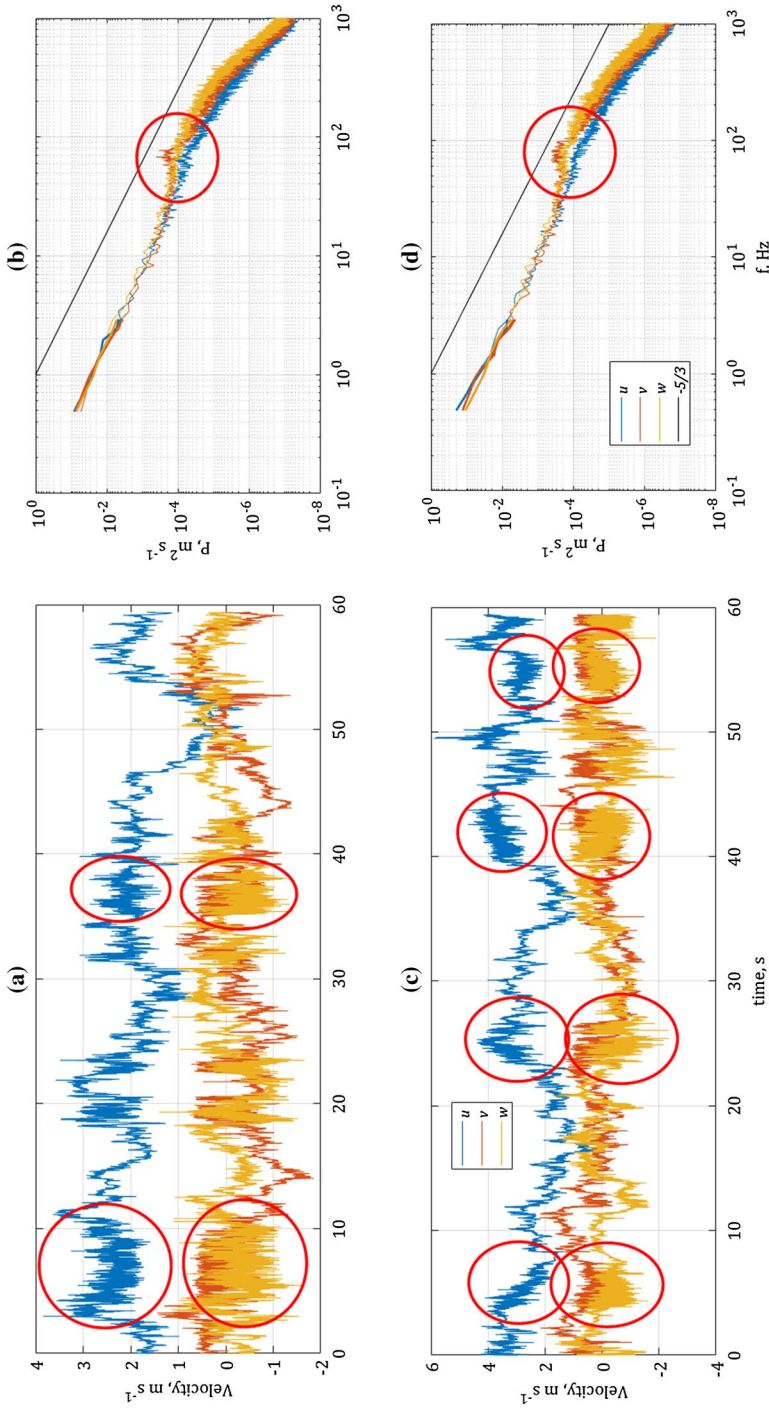


Fig. 9 Time series and spectra of two independent minutes, demonstrating the observed occurrence of bursting. The thicker lines indicate the spectral shapes from the sonic data alone. **a** Reconstructed time series; **b** respective spectra of August 10 at 9:27 am: $TI = 35.8\%$, $TKE = 0.475 \text{ m}^2 \text{ s}^{-2}$, $Sk_u = -0.341$, $\bar{\epsilon} = 0.379 \text{ m}^2 \text{ s}^{-3}$, $Re_\eta = 38.8$; **c** reconstructed time series; **d** respective spectra of August 12 at 10:57 am: $TI = 32.3\%$, $TKE = 0.748 \text{ m}^2 \text{ s}^{-2}$, $Sk_u = -0.260$, $\bar{\epsilon} = 0.482 \text{ m}^2 \text{ s}^{-3}$, $Re_\eta = 50.8$

Next the Kolmogorov (η), Taylor (L_T) and horizontal (L_H) length scales were calculated [24, 45] by

$$\eta = \left(\frac{v^3}{\bar{\epsilon}} \right)^{1/4}, \tag{4}$$

$$L_T = \sqrt{\frac{(rms(u'))^2}{\left(\frac{1}{\bar{u}} \frac{\partial u}{\partial t} \right)^2}}, \tag{5}$$

$$L_H = \frac{(rms(u'))^3}{\bar{\epsilon}}, \tag{6}$$

for all data, including the minutes at which bursting was observed. The resulting length scale values are presented in Fig. 10 alongside the representative spectra of all three components. Based on the Taylor Frozen Turbulence Hypothesis, the length scales are positioned at the respective frequencies calculated as

$$f = \frac{\bar{u}}{2\pi LS}, \tag{7}$$

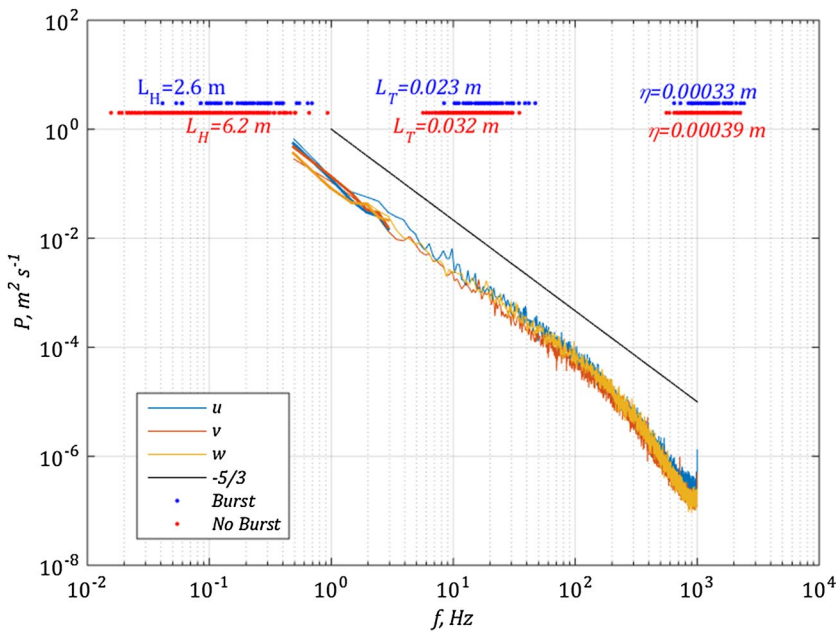


Fig. 10 Characteristic length scales calculated from the time series of velocity fluctuations for minutes with and without appearance of bursts on a representative spectral shape from Fig. 8a

where LS denotes a length scale value of a minute long record and \bar{u} denotes the mean velocity of that same minute.

Superimposing the obtained length scale values with the velocity fluctuation spectra reveals several additional interesting features of the flow. First, the η values are three times smaller than the smallest length scale resolved by the 2 kHz sampling rate. This calls for an increase by a factor of ~ 3 of the sampling rate to be used in similar future measurements to be able to obtain the fully resolved spectra. The increase in sampling frequency is achievable by the MiniCTAs used here, as their declared frequency response is up to 10 kHz. Values of L_T , signifying the largest length scale influenced by viscous dissipation, are found to be somewhat larger than the point of transition in the spectral shapes corresponding to the lower frequencies. Finally, the L_H values are in good agreement with the spectral shapes. Influence of bursting events can be readily identified in distributions of all three length scales, as values of these in minutes with bursting are consistently higher. The right shift in all length scales indicates the ability of the combo probe to capture the effects of bursting as pronounced both in time series and in spectral shapes of the velocity field component fluctuations.

Re values, calculated using the slope height as the representative length scale, were in $\sim 10^6$. In the absence of second anemometer at lower height, a use of an implicit Reynolds number, based on the η , was adopted

$$Re_\eta = \frac{\bar{u}\eta}{\nu}, \quad (8)$$

and displayed with respect to Re in Fig. 11. As the thermal forcing nature of the anabatic flow field variations was established by examination of the mean value variations in the

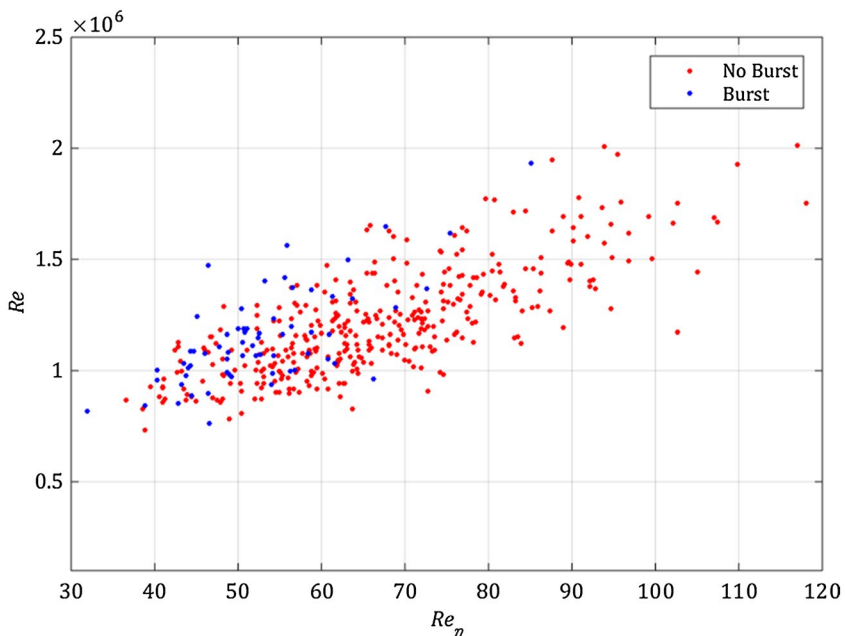


Fig. 11 Re versus Re_η of all processed minute long records without and with bursts in red and blue respectively

first part of the Sect. 4.1, Re_η hereinafter serves as an implicit representation of the thermal forces pronounced in variations of η values.

Next, the observed similarity in spectral shapes motivated suggesting a suitable normalization to collapse the data, excluding minutes in which bursting was observed. Here, a Kolmogorov universal scaling of a one-dimensional spectra [24, 40, 46, 47] was adopted to be able to compare the findings with other work available in the literature. Namely, Dubovikov and Tatarski’s theoretical model [47] (denoted as DT hereinafter) for fully developed locally isotropic turbulence was considered. It describes spectral behavior of turbulence in the viscous subrange, asymptotically connected to the inertial subrange. For this, the frequency, f , spectra were first converted to the wavenumber, k , spectra by

$$k = 2\pi f / \bar{u}. \tag{9}$$

The DT uses the dimensionless form of the velocity fluctuation power density spectrum, E ,

$$E(k\eta) = C_2(k\eta)^{-5/3} \tag{10}$$

to asymptotically represent the inertial subrange. In their analysis and based on previous studies that they examined, Dubovikov and Tatarski suggested that the constant C_2 should range from 0.42 to 0.45. Fitting the available spectral shapes of all minute long records with (10) led to C_2 of similar range of values. The results are presented in Fig. 12 as a function of implicit Reynolds number, Re_η .

Next, an asymptotic representation for the dissipation subrange was derived in [47] as

$$E(k\eta) = 60 \left(k\eta + \frac{4}{13\xi} \right) \exp(-\xi k\eta). \tag{11}$$

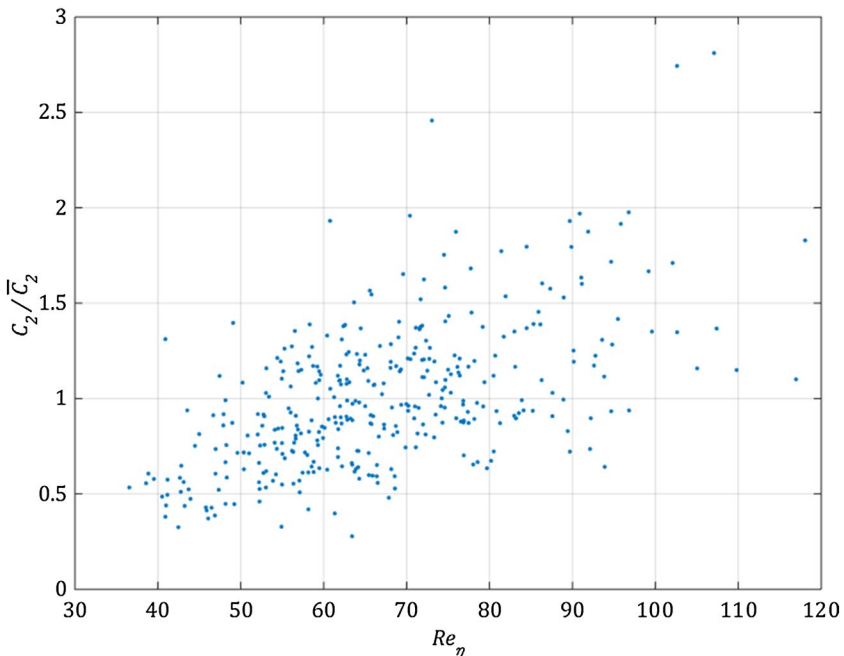


Fig. 12 Comparison of the theoretical constant $\bar{C}_2 = 0.435$ from DT [47] to C_2 values obtained by fitting the normalized spectra, with respect to Re_η

The coefficient ξ represents the asymptotic dependence of the dissipation subrange on the inertial subrange spectral shape, and according to DT can be approximated as

$$\xi_{Eq}(C_2) = 10.753 + 8.324(C_2 - 0.4164) + 4.515(C_2 - 0.4164)^2. \quad (12)$$

Hence, C_2 values obtained by fitting the spectra with (10) were used to estimate ξ_{Eq} values from (12). On the other hand, ξ_{Fit} values were obtained by directly fitting each minute spectra using (11) in the dissipation subrange only and a comparison between ξ coefficient values obtained by the two methods is plotted against the each minute Re_η in Fig. 13. The comparison shows a decreasing resemblance with the DT as Re_η increases, generally pointing toward a deviation of the examined flow from a fully developed locally isotropic turbulence characterization as the thermal forcing increased.

The normalized spectra of each velocity field component of all available minute long records are plotted in Fig. 14, presenting a tight collapse according to the adopted normalization. Hence, the DT model formulation was fitted to the collapsed curves representing the entire dataset. The spectral shapes were found to fit the model in the inertial subrange remarkably well. As for the dissipation subrange, the general fit shape was correct, but a shift from the proposed representation of ξ_{Eq} was exhibited. Data fitted coefficients are given in each plot and are somewhat smaller in all three velocity components. The findings of the fits corresponding to the DT model are summarized in Table 1. The presented exceptionally well normalized data with the model further indicates the remarkable quality of the combo obtained data in such highly turbulent flow.

Next, the behavior of TKE and TI was examined. It was calculated [24] from the time series using

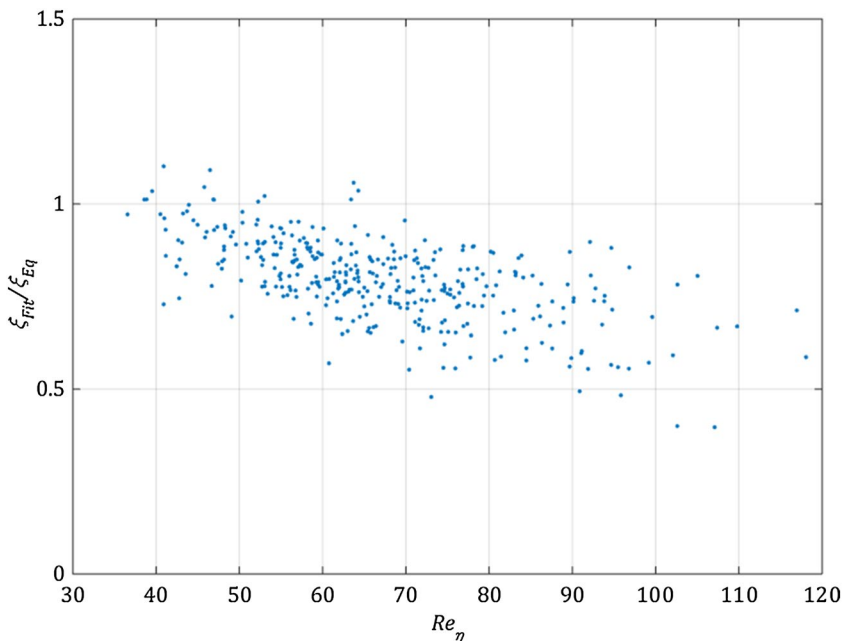


Fig. 13 Comparison of the theoretical ξ_{Eq} from DT [47] model to the values of ξ_{Fit} obtained by fitting the normalized spectra, with respect to Re_η

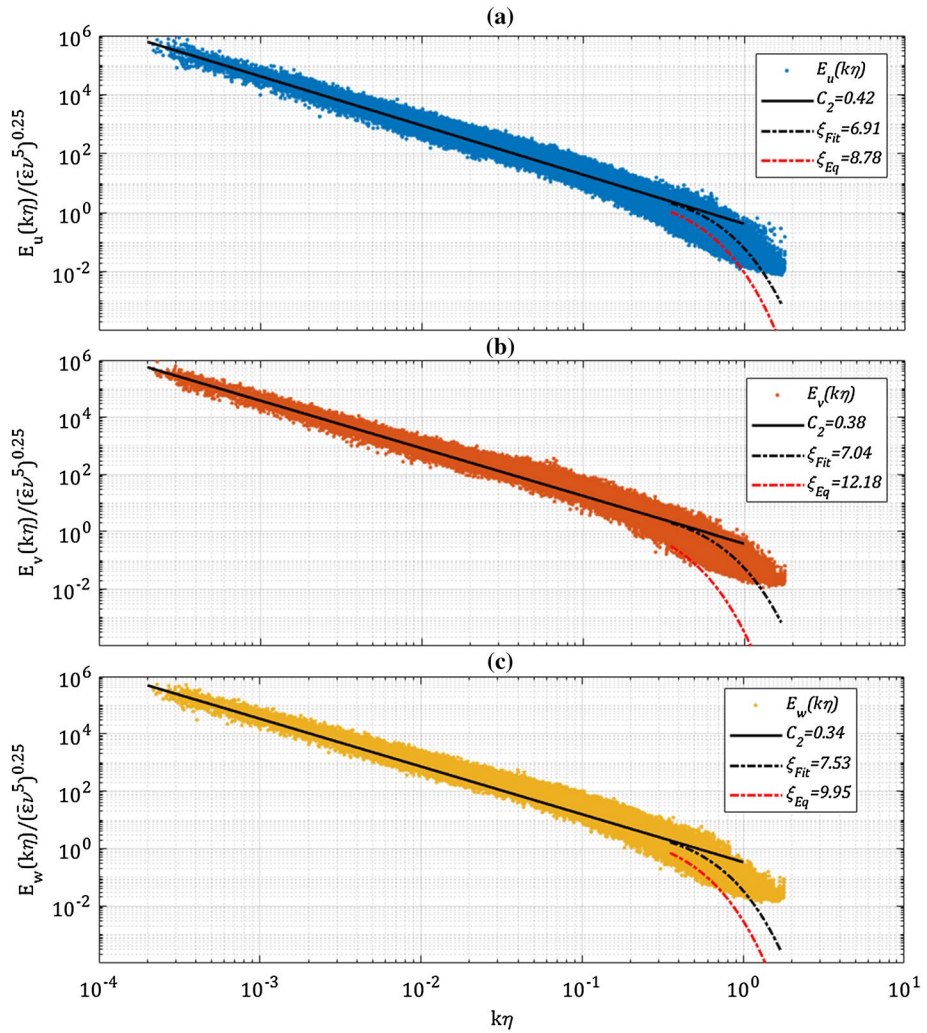


Fig. 14 Normalized power density spectra of velocity fluctuations of all available one-minute long records (blue, orange, yellow dot ensembles represent u , v , w respectively) plotted along with empirical fits according to DT. The solid black line corresponds to Eq. (10), the black dotted curve corresponds to a fit of the dot ensemble using Eq. (11), and the red dotted curve corresponds to Eqs. (11–12) using the C_2 in the legend

Table 1 Table summarizing the normalized fits for moderate slope anabatic flow

	u	v	w
C_2	0.42	0.38	0.34
ξ_{Fit}	6.91	7.04	7.53

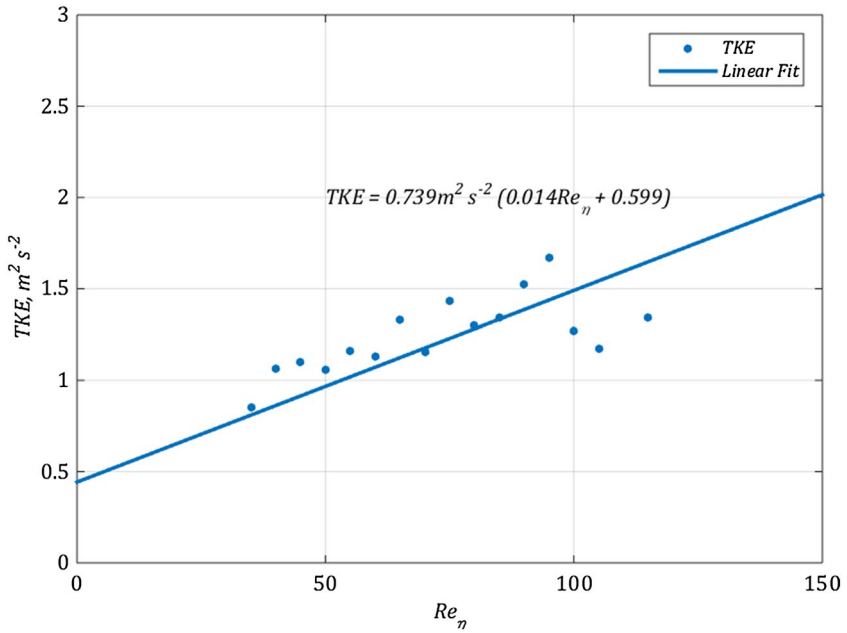


Fig. 15 Averaged TKE as a function of Re_η along with an empirical fit

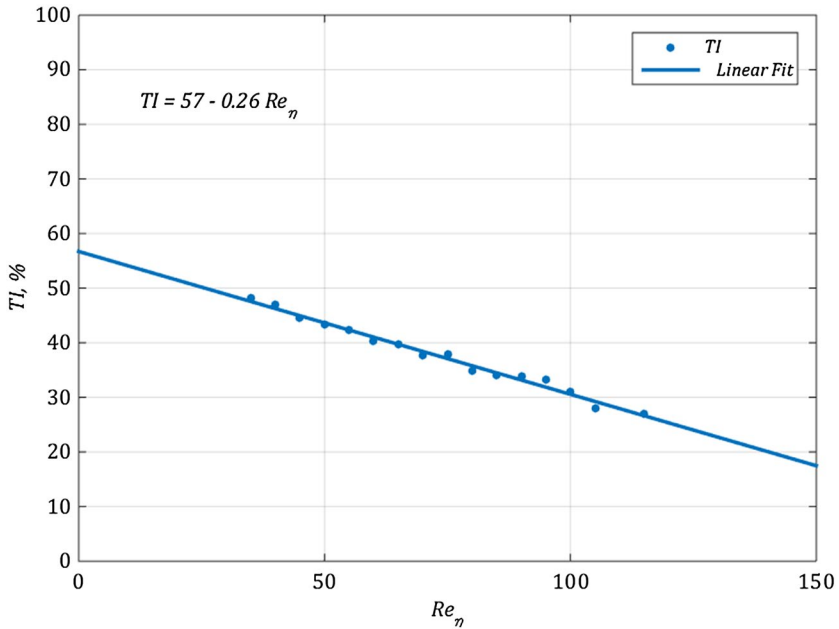


Fig. 16 Averaged TI as a function of Re_η along with an empirical fit

$$TI = \frac{\sqrt{TKE}}{\bar{u}}, \tag{13}$$

where TKE (Turbulent Kinetic Energy) is defined by

$$TKE = \frac{(u'^2 + v'^2 + w'^2)}{2}. \tag{14}$$

The velocity data were averaged over blocks of five Re_η values obtaining the empirical fits shown in Figs. 15 and 16. TKE variations were found to have a positive correlation with the Re_η while TI variations showed negative correlation since the rate of change in mean velocity is greater than that of the fluctuation intensity. As Re_η increased, the observed flow became more turbulent and the increase in TKE values was found to follow a linear trend (Fig. 15) of

$$TKE = 0.739 \text{ m}^2\text{s}^{-2} \times (0.014Re_\eta + 0.599). \tag{15}$$

The reduction in turbulence intensity along the increase of Re_η also followed a linear trend

$$TI = 57 - 0.26Re_\eta. \tag{16}$$

Next we examine the statistics obtained for the main flow velocity component, u , derivative skewness [24]

$$Sk_u = -skewness\left(\frac{\partial u}{\partial t}\right). \tag{17}$$

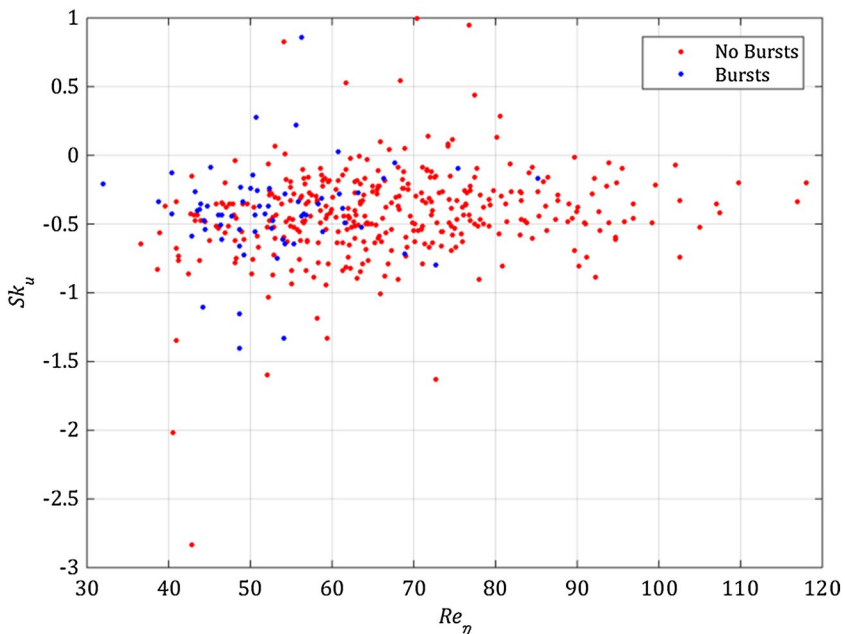


Fig. 17 Velocity derivative skewness of u with respect to Re_η of minutes without and with the appearance of bursts in red and blue respectively

Velocity derivatives skewness has a strong relation to the enstrophy generation term, and hence is regarded as one of the most important dynamical characteristics of turbulence[44]. The derivative skewness of Gaussian random process is zero by definition. Hence, determination of velocity derivative skewness in a turbulent flow helps to distinguish the real dynamical processes (turbulent fluctuations) from random noise, easily obtained in the measurements of such an unsteady process. Velocity derivative skewness values are displayed in Fig. 17 with respect to their corresponding Re_η . Skewness values were found to exhibit a significant scatter, mainly indicating the inhomogeneous nature of the examined turbulent flow. The calculated values were mostly negative, ranging between -1 and 0 , due to the non-Gaussian probability density distribution nature of the perturbations over time. An observed slight increase in Sk_u values with the increase of Re_η is indeed expected following the summarized findings in the study conducted by Sreenivasan and Antonia [48], which was based on up-to-date available field studies [49–51], lab experiments [52] and numerical models [53]. The skewness values were most commonly found to lie in the range of -0.6 to -0.1 in non-homogeneous flows due to the flow intermittency. Velocity derivative skewness often serves as an indicator of flow anisotropy, and the values obtained here average around -0.6 , indeed indicating the anisotropy of the examined flow.

The average TKE dissipation rates were calculated [24] from the time series as

$$\bar{\epsilon} = \frac{(\epsilon_u + \epsilon_v + \epsilon_w)}{3}, \tag{18}$$

where,

$$\epsilon_u = \frac{15\nu}{\bar{u}^2} \overline{\left(\frac{\partial u'}{\partial t}\right)^2}, \tag{19}$$

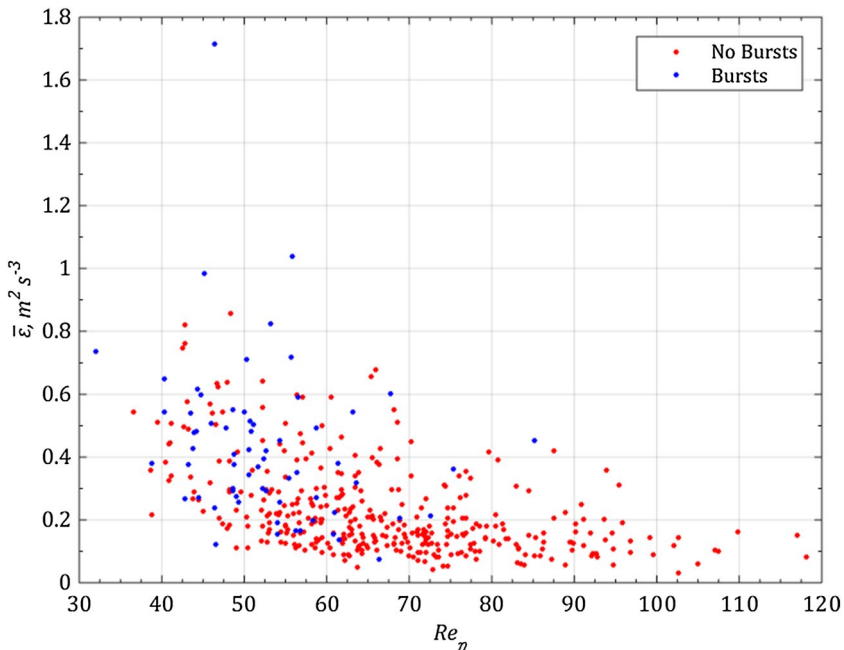


Fig. 18 Average TKE dissipation rates calculated using (18–21) of minutes without and with bursts in red and blue respectively

$$\epsilon_v = \frac{7.5v}{\bar{u}^2} \overline{\left(\frac{\partial v'}{\partial t}\right)^2}, \tag{20}$$

$$\epsilon_w = \frac{7.5v}{\bar{u}^2} \overline{\left(\frac{\partial w'}{\partial t}\right)^2}, \tag{21}$$

are presented versus Re_η in Fig. 18. Scatter of the ϵ values of all 8-day measurement data exhibits a clear decrease with Re_η , while the scatter is significant.

After observing the TKE dissipation rates obtained from the time series, additional values of the average TKE dissipation rate were obtained by fitting the spectra with the Kolmogorov canonical formulation. Accepting the Taylor Frozen Turbulence Hypothesis to represent the inertial subrange the formulation used here was of the form

$$P_u(f) = \alpha(\bar{u}/2\pi)^{2/3} \bar{\epsilon}^{2/3} f^{-5/3} \tag{22}$$

and

$$P_v(f) = P_w(f) = (4/3)P_u(f). \tag{23}$$

The value of $\alpha = 0.5$ is adopted in this study [31]. Comparison between the mean dissipation rates obtained by the two methods, direct calculation from time series and by fitting the spectra, is presented in Fig. 19.

The comparison shows ~50% difference between the TKE dissipation rates in the minutes without bursts, and greater difference of ~150% in the minutes with bursts. The ideal

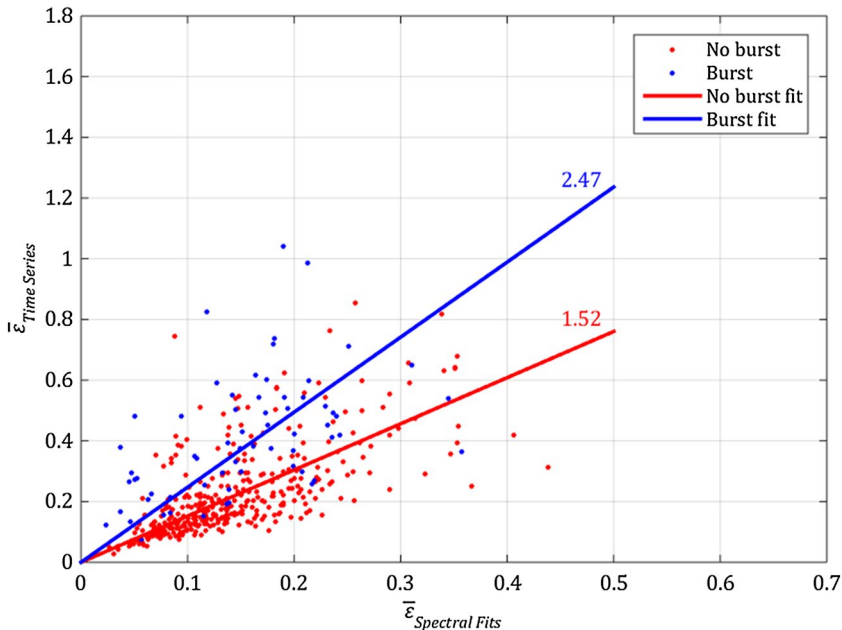


Fig. 19 Comparison between average TKE dissipation rates obtained from spectral fits (22–23) and from time series (18–21) of minutes without and with the appearance of bursts in red and blue respectively. Solid lines denote linear fit, and the values are the rates of change

flow that the equations describe should provide the same TKE dissipation rates, and the difference in obtained values depicts, once again, the anisotropic nature of the flow with the increased levels of anisotropy during minutes with bursts.

5 Conclusions

Thermally driven turbulent flows are common in the atmospheric BL, especially in anabatic/katabatic forms, and greatly influence microclimates. Obtaining various turbulence statistics, including the fully resolved spectra of velocity fluctuations, would assist in understanding the weather and climate processes and in producing accurate prediction models. However, it is difficult to capture the fine scales of such flows with the outdoor measuring instrumentation commonly available today due to unstable conditions of the flow and occasional harsh field conditions. This setup is used to examine the use of a combo probe which consists of collocated HF and sonic anemometer, while implementing the NN based in situ calibration method established in Kit et al. [32]. Continuous 8-day long field measurements of thermally driven anabatic flow on a moderate slope were performed obtaining comprehensive fine scale turbulence records. The examined flow exhibited a clear diurnal pattern with increased upslope velocity magnitude during the day and near zero velocity during night hours. Examining the temperature gradients developing on the slope and in combination with the surrounding metrological station data, it was concluded that the examined flow was driven by the diurnal solar heating cycle. Performance of the combo probe was evaluated in view of the obtained turbulent flow field statistical parameters and by comparison to a turbulent flow model due to the spectral shape similarity after choosing the appropriate scaling. The use of the combo allowed to successfully tap into the small scales of the local turbulent boundary layer flow and produce high resolution turbulence statistics, including detection of velocity fluctuation bursting events. The main findings regarding the examined anabatic flow can be summarized as follows:

- a. Development of a temporally transient anabatic flow was detected and found to be strongly correlated with the local bulk temperature difference/mean along slope buoyancy flux occurring from solar heating of the slope. The flow was characterized by implicit, Kolmogorov length scale based, Re_η values ranging between 30 and 130.
- b. The turbulence intensity of the flow was found to decrease with the increase of mean velocity, which was also accompanied by the increase of TKE. Both exhibit a linear dependency on Re_η . Additionally, the calculated values of velocity derivative skewness of the main flow direction component were mostly negative in the range between -1 and 0 . Respective empirical fits for TI and TKE dependence on Re_η were derived and presented.
- c. The power density spectra of velocity fluctuations, for all three velocity field components, were resolved to the fine scales. Approximately 15% of the records revealed the presence of the bursting phenomenon well pronounced both in the velocity time series and in the spectra.
- d. Finally, examination of the spectral shapes for all times at which the flow was oriented up the slope and excluding instances of bursting revealed a high level of similarity. The spectral data collapsed based on the Kolmogorov normalization. Comparison of the collapsed normalized spectral shapes with a Dubovikov and Tatarski [47] model showed good agreement for the inertial subrange. The deviations of our findings from the model

prediction in the viscous subrange is argued to be due to the anisotropy of the examined anabatic flow and the fact that the flow never reaches a fully developed state due to the transient nature of the thermal forcing during the day.

The data and analysis presented here mainly prove the ability of the combo probe to produce accurate measurements of high temporal and spatial resolution in temporally transient anabatic flows that are characterized by relatively high turbulence intensity and driven by unstable stratification. Moreover, the derived empirical fits, especially of the collapsed spectral shapes, can offer a useful basis for conducting future field measurements with commonly available instrumentation of low spatial/temporal resolution. Although generally site specific, the empirical fits of various turbulence statistics provided here may serve as a useful basis for more accurate numerical modelling of turbulent flows that develop in mountainous terrain due to thermal forcing.

As previously acknowledged, the combo had a measuring limitation of 120° span due to the geometric configuration of the sonic, and this limitation is being resolved by designing a new configuration to allow a full turn of the arm carrying the HF sensors. Finally, the results, and especially examination of the obtained length scales, calls for additional field measurements to be performed in various natural setups implementing higher sampling rates of at least 6 kHz to obtain fully resolved spectra of velocity field turbulent fluctuations.

Acknowledgements The authors gratefully acknowledge the support of this study by the United States–Israel Binational Science Foundation under Grant 2014075. Our greatest thanks go to Richter-Baruch family for hosting us at their property with great hospitality and providing all possible support. We also thank Prof. H.J.S. Fernando of the University of Notre Dame and Prof. David Broday of the Technion for lending us part of the equipment used in this study.

References

1. Ellis AW, Hilderbrandt ML, Thomas WM, Fernando HJS (2000) Analysis of the climatic mechanism contributing to the summertime transport of lower atmospheric ozone across metropolitan Phoenix, Arizona, USA. *Clim Res* 15:13–31. <https://doi.org/10.3354/cr015013>
2. Fernando HJS, Lee SM, Anderson J et al (2001) Urban fluid mechanics: air circulation and contaminant dispersion in cities. *Environ Fluid Mech* 1:107–164. <https://doi.org/10.1023/A:1011504001479>
3. Faller AJ (1965) Large eddies in the atmospheric boundary layer and their possible role in the formation of cloud rows. *J Atmos Sci* 22:176–184
4. Otarola S, Dimitrova R, Leo L, et al (2016) On the role of the Andes on weather patterns and related environmental hazards in Chile. AMS
5. Whiteman CD (2000) *Mountain meteorology: fundamentals and applications*. Oxford University Press, New York
6. Princevac M, Fernando HJS (2007) A criterion for the generation of turbulent anabatic flows. *Phys Fluids* 19:1051021–1051027. <https://doi.org/10.1063/1.2775932>
7. Chow FK, De Wekker SFJ, Snyder (2015) Mountain weather and research forecasting. <https://doi.org/10.1017/cbo9781107415324.004>
8. Oldroyd HJ, Pardyjak ER, Higgins CW, Parlange MB (2016) Buoyant turbulent kinetic energy production in steep-slope katabatic flow. *Boundary-Layer Meteorol*. <https://doi.org/10.1007/s10546-016-0184-3>
9. Monti P, Fernando HJS, Princevac M et al (2002) Observations of flow and turbulence in the nocturnal boundary layer over a slope. *J Atmos Sci* 59:2513–2534. [https://doi.org/10.1175/1520-0469\(2002\)059%3c2513:OOFATI%3e2.0.CO;2](https://doi.org/10.1175/1520-0469(2002)059%3c2513:OOFATI%3e2.0.CO;2)
10. Demko JC, Geerts B, Miao Q, Zehnder JA (2009) Boundary layer energy transport and cumulus development over a heated mountain: an observational study. *Am Meteorol Soc Mon Weather Rev* 137:447–468. <https://doi.org/10.1175/2008MWR2467.1>

11. Fernando HJS (2010) Fluid dynamics of urban atmospheres in complex terrain. *Annu Rev Fluid Mech* 42:365–389. <https://doi.org/10.1146/annurev-fluid-121108-145459>
12. Choi W, Faloona IC, McKay M et al (2011) Estimating the atmospheric boundary layer height over sloped, forested terrain from surface spectral analysis during BEARPEX. *Atmos Chem Phys* 11:6837–6853. <https://doi.org/10.5194/acp-11-6837-2011>
13. Fernando HJS, Pardyjak ER, Di Sabatino S, et al (2015) The materhorn : unraveling the intricacies of mountain weather. *Bull Am Meteorol Soc.* <https://doi.org/10.1175/bams-d-13-00131.1>
14. Hunt JCR, Fernando HJS, Princevac M (2003) Unsteady thermally driven flows on gentle slopes. *J Atmos Sci* 60:2169–2182. [https://doi.org/10.1175/1520-0469\(2003\)060%3c2169:UTDFOG%3e2.0.CO;2](https://doi.org/10.1175/1520-0469(2003)060%3c2169:UTDFOG%3e2.0.CO;2)
15. Reuten C, Steyn DG, Allen SE (2007) Water tank studies of atmospheric boundary layer structure and air pollution transport in upslope flow systems. *J Geophys Res Atmos* 112:1–17. <https://doi.org/10.1029/2006JD008045>
16. Reuten C (2008) Upslope flow systems: scaling, structure, and kinematics in tank and atmosphere. VDM Verlag Dr. Müller, Saarbrücken
17. Moroni M, Giorgilli M, Cenedese A (2014) Experimental investigation of slope flows via image analysis techniques. *J Atmos Solar-Terr Phys* 108:17–33. <https://doi.org/10.1016/j.jastp.2013.12.008>
18. Schumann U (1990) Large-eddy simulation of the up-slope boundary layer. *Q J R Meteorol Soc* 116:637–670. <https://doi.org/10.1256/smsqj.49306>
19. Noppel H, Fiedler F (2002) Mesoscale heat transport over complex terrain by slope winds- a conceptual model and numerical simulations. *Boundary-Layer Meteorol* 104(104):73–97
20. Rampanelli G, Zardi D, Rotunno R (2004) Mechanisms of up-valley winds. *J Atmos Sci* 61:3097–3111. <https://doi.org/10.1175/JAS-3354.1>
21. Fedorovich E, Shapiro A (2009) Structure of numerically simulated katabatic and anabatic flows along steep slopes. *Acta Geophys* 57:981–1010. <https://doi.org/10.2478/s11600-009-0027-4>
22. Serafin S, Zardi D (2010) Structure of the atmospheric boundary layer in the vicinity of a developing upslope flow system: a numerical model study. *J Atmos Sci* 67:1171–1185. <https://doi.org/10.1175/2009JAS3231.1>
23. Geerts B, Raymond DJ, Grubišić V, Davis CA, Barth MC, Detwiler A, Klein PM, Lee W, Markowski PM, Mullendore GL, Moore JA (2018) Recommendations for in situ and remote sensing capabilities in atmospheric convection and turbulence. *Am Meteorol Soc.* <https://doi.org/10.1175/bams-d-17-0310.1>
24. Pope SB (2000) *Turbulent flows*. Cambridge University Press, New York
25. Hayashi T (1992) Gust and downward momentum transport in the atmospheric surface layer. *Boundary-Layer Meteorol* 58:33–49
26. McNaughton K, Laubach J (2000) Power spectra and cospectra for wind and scalars in a disturbed surface layer at the base of an advective inversion. *Boundary-layer Meteorol* 96:143–185. <https://doi.org/10.1023/A:1002477120507>
27. Lothon M, Lenschow DH, Mayor SD (2009) Doppler lidar measurements of vertical velocity spectra in the convective planetary boundary layer. *Boundary-Layer Meteorol* 132:205–226. <https://doi.org/10.1007/s10546-009-9398-y>
28. Krishnamurthy R, Calhoun R, Billings B, Doyle J (2011) Wind turbulence estimates in a valley by coherent Doppler lidar. *Meteorol Appl* 18:361–371. <https://doi.org/10.1002/met.263>
29. Potter H, Graber HC, Williams NJ et al (2015) In situ measurements of momentum fluxes in typhoons. *J Atmos Sci* 72:104–118. <https://doi.org/10.1175/JAS-D-14-0025.1>
30. Oncley SP, Friehe CA, Larue JC et al (1996) Surface layer fluxes profiles and turbulence measurements over uniform terrain under near neutral conditions. *J Atmos Sci* 53:1029–1044
31. Kaimal JC, Finnigan JJ (1994) *Atmospheric boundary layer flows: their structure and measurement*. Book. [https://doi.org/10.1016/0021-9169\(95\)90002-0](https://doi.org/10.1016/0021-9169(95)90002-0)
32. Kit E, Cherkassky A, Sant T, Fernando HJS (2010) In situ calibration of hot-film probes using a collocated sonic anemometer: implementation of a neural network. *J Atmos Ocean Technol* 27:23–41. <https://doi.org/10.1175/2009JTECHA1320.1>
33. Vitkin L, Liberzon D, Grits B, Kit E (2014) Study of in situ calibration performance of co-located multi-sensor hot-film and sonic anemometers using a ‘virtual probe’ algorithm. *Meas Sci Technol* 25:75801. <https://doi.org/10.1088/0957-0233/25/7/075801>
34. Kit E, Liberzon D (2016) 3D-calibration of three- and four-sensor hot-film probes based on collocated sonic using neural networks. *Meas Sci Technol* 27:95901. <https://doi.org/10.1088/0957-0233/27/9/095901>
35. Kit E, Hocut CM, Liberzon D, Fernando HJS (2017) Fine-scale turbulent bursts in stable atmospheric boundary layer in complex terrain. *J Fluid Mech* 833:745–772. <https://doi.org/10.1017/jfm.2017.717>

36. Turnipseed AA, Anderson DE, Burns S et al (2004) Airflows and turbulent flux measurements in mountainous terrain: Part 2: Mesoscale effects. *Agric For Meteorol* 125:187–205. <https://doi.org/10.1016/j.agrformet.2004.04.007>
37. Hocut CM, Liberzon D, Fernando HJS (2015) Separation of upslope flow over a uniform slope. *J Fluid Mech* 775:266–287. <https://doi.org/10.1017/jfm.2015.298>
38. Stull RB (1988) An introduction to boundary layer meteorology. Book. <https://doi.org/10.1007/978-94-009-3027-8>
39. Whiteman CD (1990) Observations of thermally developed wind systems in mountainous terrain. Chapter 2. In: *Atmospheric processes over complex terrain*, Boston, pp 5–42
40. Saddoughi SG, Veeravalli SV (1994) Local isotropy in turbulent boundary layers at high Reynolds number. *J Fluid Mech* 268:333–372. <https://doi.org/10.1017/s0022112094001370>
41. Falkovich G (1994) Bottleneck phenomenon in developed turbulence. *Phys Fluids* 6:1411–1414. <https://doi.org/10.1063/1.868255>
42. Tatarskii VI (2005) Use of the 4/5 Kolmogorov equation for describing some characteristics of fully developed turbulence. *Phys Fluids* 17:03511001–03511012. <https://doi.org/10.1063/1.1858531>
43. Kim H, Kline S, Reynolds W (1971) The production of turbulence near a smooth wall in a turbulent boundary layer. *J Fluid Mech* 50:133–160
44. Davidson PA (2004) *Turbulence an introduction for scientists and engineers*. Oxford University Press, New York
45. Brethouwer G, Billant P, Lindborg E, Chomaz J-M (2007) Scaling analysis and simulation of strongly stratified turbulent flows. *J Fluid Mech* 585:343–368. <https://doi.org/10.1017/S0022112007006854>
46. Kolmogorov AN (1941) The local structure of turbulence in incompressible viscous fluid for very large Reynolds numbers. *Proc Acad Sci USSR Geochem Sect* 30:299–303. <https://doi.org/10.1098/rspa.1991.0075>
47. Dubovikov M, Tatarskii VI (1987) Calculation of the asymptotic form of the spectrum of locally isotropic turbulence in the viscous range. 66:1136–1141
48. Sreenivasan KR, Antonia RA (1997) The phenomenology of small-scale turbulence. *Annu Rev Fluid Mech* 29:435–472. <https://doi.org/10.1146/annurev.fluid.29.1.435>
49. Gibson CH, Stegen GR, Williams RB (1970) Statistics of the fine structure of turbulent velocity and temperature fields measured at high Reynolds number. *J Fluid Mech* 41:153–167. <https://doi.org/10.1017/S0022112070000551>
50. Wyngaard JC, Tennekes H (1970) Measurements of the small-scale structure of turbulence at moderate Reynolds numbers. *Phys Fluids* 13:1962–1969. <https://doi.org/10.1063/1.1693192>
51. Antonia R, Satyaprakash B, Chambers A (1981) Reynolds number dependence of high-order moments of the streamwise turbulent velocity derivative. *Bound Layer Meteorol* 21:159–171
52. Antonia R, Satyaprakash B, Hussain A (1982) Statistics of fine-scale velocity in turbulent plane and circular jets. *J Fluid Mech* 119:55–89. <https://doi.org/10.1017/S0022112082001268>
53. Jiménez J, Wray AA, Saffman PG, Rogallo RS (1993) The structure of intense vorticity in isotropic turbulence. *J Fluid Mech* 255:65–90. <https://doi.org/10.1017/S0022112093002393>

Publisher's Note Springer Nature remains neutral with regard to jurisdictional claims in published maps and institutional affiliations.